



HAL
open science

New insights into thermomechanical behavior of GeTe thin films during crystallization

Marion Gallard, Mohamed Salah Amara, Magali Putero, Nelly Burle, Christophe Guichet, Stéphanie Escoubas, Marie-Ingrid Richard, Cristian Mocuta, Rebbeca R Chahine, Mathieu Bernard, et al.

► To cite this version:

Marion Gallard, Mohamed Salah Amara, Magali Putero, Nelly Burle, Christophe Guichet, et al.. New insights into thermomechanical behavior of GeTe thin films during crystallization. *Acta Materialia*, 2020, 191, pp.60-69. 10.1016/j.actamat.2020.04.001 . hal-02903073

HAL Id: hal-02903073

<https://hal.science/hal-02903073v1>

Submitted on 22 Aug 2022

HAL is a multi-disciplinary open access archive for the deposit and dissemination of scientific research documents, whether they are published or not. The documents may come from teaching and research institutions in France or abroad, or from public or private research centers.

L'archive ouverte pluridisciplinaire **HAL**, est destinée au dépôt et à la diffusion de documents scientifiques de niveau recherche, publiés ou non, émanant des établissements d'enseignement et de recherche français ou étrangers, des laboratoires publics ou privés.



Distributed under a Creative Commons Attribution - NonCommercial 4.0 International License

New insights into thermomechanical behavior of GeTe thin films during crystallization

M. Gallard^{1,2}, M. S. Amara¹, M. Putero^{1*}, N. Burle¹, C. Guichet¹, S. Escoubas¹, M.-I. Richard^{1,3}, C. Mocuta², R. R. Chahine⁴, M. Bernard⁴, P. Kowalczyk⁴, P. Noé⁴, O. Thomas¹

¹ Aix-Marseille Université, CNRS, IM2NP UMR 7334, Campus de St-Jérôme, 13397 Marseille Cedex 20, France

² Synchrotron SOLEIL, l'Orme des Merisiers, Saint-Aubin–BP 48, 91192 Gif-sur-Yvette, France

³ ID01/ESRF, The European Synchrotron, 71 rue des Martyrs, 38043 Grenoble, France.

⁴ Université Grenoble Alpes, CEA-LETI, MINATEC, 17 rue des Martyrs, 38054 Grenoble, France.

*Corresponding author: Magali Putero

Key-word: phase change materials, GeTe, chalcogenide, precipitation, stress, crystallization, sheet resistance, PCRAM

ABSTRACT

In this work, we reexamine Ge rejection in Ge-rich GeTe thin films with a slight deviation from stoichiometry using a unique combination of *in situ* measurements: curvature and x-ray diffraction as well as electrical resistance and x-ray diffraction and reflectivity during annealing. This unique combination of several experiments performed simultaneously on a synchrotron beamline allows to monitor *in situ*, during the crystallization and phase transformation, the microstructure, the strain and the stress changes, as well as electrical properties of GeTe films. Structural, electrical and thermomechanical evolutions of the GeTe thin films upon annealing are shown to follow three different steps. Stage I, before crystallization, is characterized by a tensile stress variation and a small decrease of the mass density. Stage II corresponds to the rhombohedral α GeTe phase crystallization leading to an abrupt tensile stress jump (+72 MPa), a mass density increase, and followed by a slight compressive stress evolution. During stage III, Ge crystallization is observed leading to a compressive stress jump (-54 MPa), an abrupt increase in α GeTe lattice spacing and diffracted intensity, whereas α GeTe diffraction peak widths decrease. During cooling a thermoelastic behavior is observed. A detailed analysis of stage III (Ge precipitation and crystallization) is performed and discussed regarding structural, stress, microstrain, electrical and thermomechanical properties. In particular, this study reveals that crystalline Ge precipitation results in important changes (volume of the unit cell, homogeneity of lattice spacing, average stress ...) in the surrounding GeTe matrix. Different scenarios are proposed to understand these results.

39 1. Introduction

40 One of the leading materials for new emerging non-volatile memories are phase change materials
41 (PCMs). PCMs have been successfully employed in optical memories such as DVD-RAM since the
42 1990s and more recently in the commercial production of electronic non-volatile phase-change
43 random access memory (PCRAM)[1–3]. They are also deeply studied by academia for numerous new
44 application and for the complex physics associated with their properties[4,5]. PCMs are characterized
45 by a unique combination of properties[6] and continue to pose challenges for very basic fundamental
46 research[7,8]. They exist in an amorphous and a crystalline phase with huge different optical and
47 electrical properties caused by an unusual change of bonding when the amorphous phase is
48 crystallized[8,9]. The amorphous phase exhibits in general high electrical resistivity and low optical
49 reflectance, and the reverse properties are observed in the crystalline phase[10]. The capability to
50 change the phase of such a material in very short times (nanoseconds) and repeatedly between the two
51 phases makes PCMs ideal candidates for data storage. Among the large class of PCMs, the two
52 prototypes and most studied materials are the $\text{Ge}_2\text{Sb}_2\text{Te}_5$ and GeTe chalcogenide alloys. They both
53 belong to the GeTe– Sb_2Te_3 pseudo-binary diagram[11] and GeTe was one of the first binary alloy
54 showing fast recrystallization and good optical contrast.

55 The Ge-enrichment of PCM alloys allows to stabilize the amorphous state resulting in a better thermal
56 stability and data retention[12,13]. However, in such non-stoichiometric alloy, both the phase
57 separation upon crystallization and the strain energy of crystallites nucleated in amorphous matrix
58 have been shown to play a crucial role for PCRAM performances[14]. Ge segregation in Ge-rich
59 alloys is for example at the origin of failure mechanisms in PCRAM devices[15,16]. Previous studies
60 about Ge-enrichment in Ge-Sb, Ge-Te, and GeSbTe alloys have shown that the excess Ge always
61 precipitates and crystallizes above the alloy crystallization temperature (T_x). In Ge-Sb alloy, Ge
62 enrichment is shown to increase T_x [17], the crystallization of GeSb being followed by Ge precipitation
63 and crystallization[18]. Even without Ge-enrichment, the annealing of as-deposited amorphous
64 $\text{Ge}_x\text{Sb}_{1-x}$ alloy ($x < 0.4$) leads to Sb-rich phase crystallization followed by the formation of amorphous
65 Ge regions that crystallize afterward, the Ge crystallization occurring thus at relatively low
66 temperature[19,20]. In other systems such as Ge-rich GeSbTe or Ge-rich GaSb alloy[21], the
67 precipitation and crystallization of pure Ge is also observed at temperatures slightly higher than T_x , Ge
68 grains (~10nm) being embedded in the GeSbTe matrix[22]. Concerning Ge-rich $\text{Ge}_x\text{Te}_{1-x}$ thin films
69 (with $0.5 < x < 0.66$), the precipitation and crystallization of the excess element are usually
70 observed[23] at a temperature larger than the crystallization temperature (T_x) of rhombohedral GeTe
71 [3,16,24]. However, very few studies explain such Ge precipitation and crystallization at a temperature
72 around 300°C, that is much lower than the Ge crystallization temperature[25]. Moreover the
73 description of the crystallization process often suffer from a lack of accurate *in situ* measurements,
74 most experimental studies producing *ex situ* analysis after annealing at different temperatures. In Ge-
75 Sb alloys, previous studies[17,26] have discussed metal-induced crystallization as a possible
76 mechanism for the Ge crystallization and precipitation: they describe a process that starts by
77 crystallization and diffusion of Sb in a Ge–Sb matrix. Sb diffusion could induce Ge crystallization
78 through Ge–Sb bond breaking comparable to a metal-induced crystallization process. In $\text{Ge}_{0.6}\text{Te}_{0.4}$, Yi
79 et al.[27] have shown by *ab initio* molecular dynamics simulation that Ge atoms prefer to clump

80 together and form Ge tetrahedral clusters in the amorphous phase, possibly explaining experimental
81 findings of segregation of crystalline Ge grains. In $\text{Ge}_{0.63}\text{Te}_{0.37}$ thin films, Carria et al.[28] have
82 evidenced the presence of amorphous Ge precipitates at the initial stage of the crystallization, the
83 GeTe crystalline grains subsequently acting as a seed for Ge crystallization. The Ge precipitates were
84 shown to be nestled inside the GeTe grains with some aligned crystal orientation. In this study, the
85 atomic interdiffusivity was also estimated near the crystallization temperature and Tellurium was
86 shown to be likely the diffusing species.

87 In this work, we reexamine Ge rejection in Ge-rich GeTe thin films with a slight deviation from
88 stoichiometry using unique combinations of *in situ* measurements: curvature and x-ray diffraction as
89 well as electrical resistance and x-ray diffraction and reflectivity during annealing. This unique
90 combination of both experiments performed simultaneously on a synchrotron beamline allows to
91 monitor *in situ* during the crystallization and phase transformation the microstructure, the strain and
92 the stress evolutions, as well as the electrical properties in thin PCM films[29]. Because of its peculiar
93 sensitivity, this experimental *in situ* study gives new insights into the thermomechanical behavior of
94 GeTe thin films during crystallization and Ge precipitation and the delicate interplay between
95 composition and stress in these films.

96

97 **2. Experimental procedures**

98 100 nm thick GeTe film were deposited on 200 mm Si(001) substrates by magnetron sputtering from a
99 nominally stoichiometric GeTe target. While for *in situ* X-ray reflectivity measurements 700 micron-
100 thick substrates were used, 100 micron-thick silicon substrates were used for macroscopic curvature
101 measurements to increase substrate bending under the film influence. The films were capped with 10
102 nm of TaN or SiN to prevent surface oxidation. After the deposition process, the film composition was
103 assessed by means of Rutherford Backscattering Spectrometer (RBS) and Wavelength Dispersive X-
104 ray Fluorescence (WDXRF), yielding slightly Ge-rich $\text{Ge}_{0.52\pm 0.01}\text{Te}_{0.48\pm 0.01}$ layers.

105 Samples were *in situ* annealed (2 °C/min) under nitrogen atmosphere in a chamber specially designed
106 to simultaneously perform X-ray scattering (diffraction, XRD and/or reflectivity, XRR) and wafer
107 curvature measurements[29,30]. The maximum annealing temperature was 400°C and the cooling rate
108 was set to 5°C/min. The heating stage from Anton Paar® was equipped with a 300 µm thick
109 PolyEtherEtherKetone (PEEK) dome for X-ray measurements and an optical quartz viewport to let the
110 laser beam through for optical measurements of sample curvature. The furnace was mounted on the
111 six-circle diffractometer (Kappa geometry) of the DiffAbs beamline at SOLEIL synchrotron. Square
112 pieces of samples, about 10 × 10 mm² in size, were cut from the wafer and directly posed on the
113 heating plate without clamping, so that they were free to bend during curvature measurements. The
114 XRD patterns were recorded at a fixed grazing angle $\omega = 5^\circ$ using a two-dimensional X-ray hybrid
115 pixel array detector, XPAD[31,32]. An incident photon energy $E = 16$ keV or $E = 18$ keV was chosen
116 in order to measure a large angular range and to optimize combined XRD and XRR measurements.
117 The diffracted intensities as a function of the diffracted angles 2θ were obtained after 1D azimuthal
118 integration and by applying geometrical corrections and background subtraction[33,34]. It is worth
119 emphasizing that in these experimental conditions with scattering angle ranging (2θ) between 12 and

120 24° the diffracting plane normals lie between 1 and 7° from the surface normal. Hence the information
121 accessed by diffraction (for ex. interplanar distances, grain sizes...) is basically along the normal to the
122 film surface. The XRR patterns were recorded in θ -2 θ geometry, with a point detector, in less than 1
123 minute. At each temperature, before performing XRR, the sample surface was automatically realigned
124 in the X-ray beam (height and zero of the incidence angle). The data processing for XRR patterns to
125 extract both film thickness and mass density is detailed in the Supplemental Material.

126 Simultaneously to the X-ray data acquisition, the substrate curvature was monitored to get insight into
127 the film stress as detailed in Ref.[29,35]. This has been performed with a kSA® multi-beam optical
128 sensor (MOS), which uses an array of parallel laser beams generated by a 658 nm wavelength laser
129 beam crossing two parallel plates etalons. The sample surface, perpendicular to the incident laser
130 beams, reflects these laser spots, which are captured by a charge-coupled detector. The MOS system is
131 first calibrated with an optical flat mirror. The spacing between the spots reflected by the flat mirror is
132 used as a reference. The deformation of the array after reflection from the sample allows determining
133 the sample curvature along two directions:

$$134 \quad \kappa = \frac{\cos \alpha}{2L} \frac{d-d_0}{d_0} \quad (1)$$

135 where L and α are respectively the sample-to-detector (CCD camera) distance and the incident angle
136 of the beam on the sample surface. d and d_0 are respectively the distance between the laser spots
137 before and after reflection from the sample. Knowing the substrate thickness h_s and its biaxial
138 modulus M_s the force per unit length applied by the film on the substrate can be deduced:

$$139 \quad F = M_s \frac{h_s^2}{6} (\kappa - \kappa_0) \quad (2)$$

140 where κ_0 is the curvature of the bare substrate surface. Formula (2) is called Stoney equation and is
141 valid provided the film thickness is small enough as compared with the substrate thickness and that the
142 substrate remains in the small deformation regime (bow should remain smaller than the substrate
143 thickness). Both conditions are met in the samples investigated in this work. In the case of a
144 homogeneous in-plane stress σ_f in the film of thickness h_f , the force per unit length F writes:

$$145 \quad F = \sigma_f h_f \quad (3)$$

146 In this work, we used as κ_0 in formula (2) the initial room-temperature curvature of the film-substrate
147 system. Hence the force F is a relative force with respect to the initial situation, which includes bare
148 substrate curvature and residual stress in the as-deposited film.

149 Simultaneous *in situ* XRD, XRR and sheet resistance (R_s) measurements were also performed using
150 another dedicated vacuum chamber (10^{-5} mbar) equipped with a heating stage and an aligned 4-point
151 probe sheet resistance set-up[10,36]. For such experiment, Si(100) substrates covered by an insulating
152 500 nm thick thermal SiO₂ layer were used. The heating chamber was mounted on the six-circle
153 diffractometer of the DiffAbs beamline at SOLEIL synchrotron, and XRD, XRR and R_s were recorded
154 during the sample annealing using same constant heating and cooling rate as previously described.
155 Both XRD and XRR measurements were performed as described above; simultaneously to the
156 collection of XRR and XRD data, the sheet resistance was measured: the current was supplied by a
157 Keithley 6220 precision current source, while the voltage was measured using a Keithley 2182A
158 nanovoltmeter, with the 4-point probes lying on the sample surface.

159

160 3. STABLE PHASES OF GeTe AND CRYSTALLOGRAPHY OF THE LOW 161 TEMPERATURE α PHASE

162 According to the equilibrium phase diagram[37] $\text{Ge}_{1-x}\text{Te}_x$ crystallizes in three different structures
163 under atmospheric pressure. The homogeneity domain at 703 K is 50.3 – 51.5 Te at%. At room
164 temperature, the stable phase is rhombohedral αGeTe ($R\bar{3}m$ space group) on the Ge-rich side and
165 orthorhombic γGeTe (SnS structure) on the Te-rich side. Above 640-700 K the stable phase is cubic
166 βGeTe ($\text{Fm}\bar{3}m$, NaCl type). There are some controversies about the nature of this α - β transition
167 whether it is a Peierls transition or an order-disorder transition[6]. βGeTe may also be stabilized at
168 room temperature under high pressure[38]. It is reported that the dominant non-stoichiometric defects
169 in αGeTe are double ionized vacancies on the Ge sublattice[37].

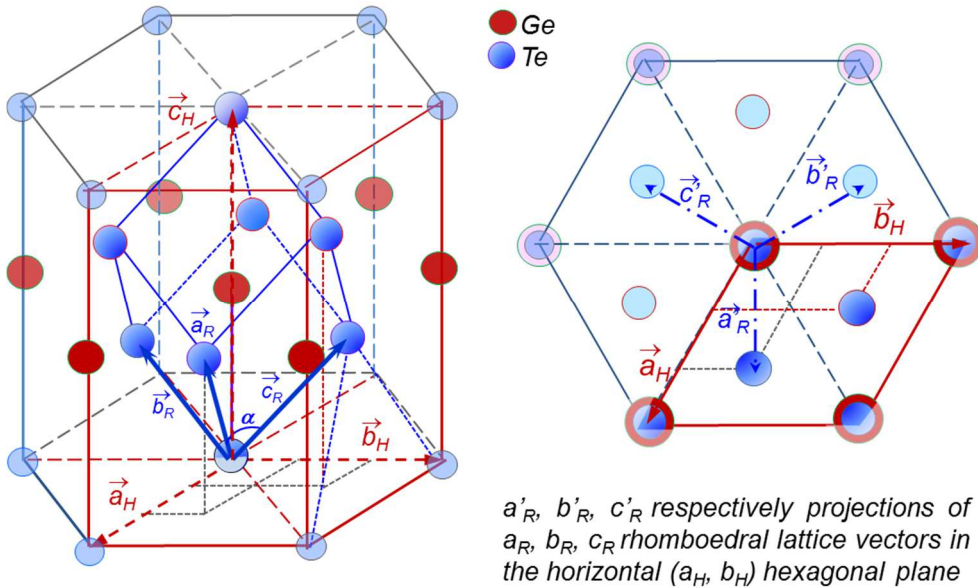
170 At room temperature, the rhombohedral primitive unit cell αGeTe has the following lattice
171 parameters[39]: $a_R = 0.4281$ nm and $\alpha = 58.359^\circ$. It is often convenient to use a multiple ($M=3$)
172 hexagonal unit cell whose lattice parameters are related to the rhombohedral cell parameters by:

173

$$174 \quad a_H = 2a_R \sin(\alpha/2)$$
$$175 \quad \text{and } c_H = a_R \sqrt{3 + 6 \cos \alpha} \quad (4)$$

176

177 respectively $a_R = \frac{1}{3} \sqrt{3a_H^2 + c_H^2} \quad (5)$



178

179 *Figure 1* : Rhombohedral (in blue) versus hexagonal (in red) lattices; The basis is a $\text{Ge}(0, 0, 0)$ - $\text{Te}(0.475, 0.475,$
180 $0.475)$ pair in the rhombohedral cell, or $\text{Ge}(0, 0, 0) - \text{Te}(0, 0, 1/2)$ in the hexagonal cell. Ge atoms are in blue; Te
181 atoms are in red, for clarity not all of them are represented.

182

183 Hence the hexagonal parameters are $a_H = 0.4174$ nm ; $c_H = 1.0614$ nm (Fig.1). Slightly different values
184 are reported by Chattopadhyay *et al.*[40]: $a_H = 0.4164$ nm ; $c_H = 1.069$ nm

185 In this article, the hexagonal simplest cell ($M=3$, in red in fig.1) is chosen to describe the lattice. As
186 usual in the literature on GeTe, the three indices (hkl) notation is used (instead of $(h k i l)$).

187 It is worth noting that these α GeTe hexagonal lattice parameters yield very close interplanar distances
188 for non-equivalent lattice planes: for example, (003)/(101), as well as (104)/(110) planes exhibit very
189 similar interplanar distances (see Table 1). These small differences get even smaller when the
190 temperature increases because of the anisotropic thermal expansion of α GeTe.

191 Thermal expansion of α GeTe has been measured by Chattopadhyay *et al.*[40] on single crystals. Using
192 this data, one can extract the hexagonal thermal expansion coefficients α_a and α_c between 295 and 665
193 K: $\alpha_a = 3.19 \times 10^{-5} \text{ K}^{-1}$ and $\alpha_c = -2.05 \times 10^{-5} \text{ K}^{-1}$. The volumetric thermal expansion is $\alpha_v = 4.33 \times 10^{-5} \text{ K}^{-1}$,
194 and the average linear thermal expansion coefficient is $\alpha_v/3 = 1.44 \times 10^{-5} \text{ K}^{-1}$. From temperature-
195 dependent powder diffraction measurements[41], Chatterji reports $\alpha_v = 4.59 \times 10^{-5} \text{ K}^{-1}$, which yields
196 $\alpha_v/3 = 1.53 \times 10^{-5} \text{ K}^{-1}$. These measurements are in agreement with the earlier ones performed by
197 Wiedemeier[42] and the most recent ones reported by Tran[43].

198 This high anisotropy in thermal expansion triggers the thermal evolution of lattice spacings. In the
199 absence of stress, the thermal expansion of (hkl) lattice planes writes:

$$200 \quad \alpha_{hkl} = \alpha_a - \left(\frac{a_0}{c_0}\right)^2 \frac{l^2}{\frac{4}{3}(h^2+k^2+hk) + \left(\frac{a_0}{c_0}\right)^2 l^2} (\alpha_a - \alpha_c) \quad (6)$$

201 The bulk modulus of GeTe has been measured by Onodera[38] as 49.9 GPa. The six independent
202 elastic constants have been calculated within the density functional theory approximation[44,45]. The
203 calculated extreme values of Young modulus show that R3m GeTe exhibits a strong elastic
204 anisotropy: $48 \text{ GPa} \leq E \leq 132 \text{ GPa}$ [44] or $37 \text{ GPa} \leq E \leq 119 \text{ GPa}$ [45]. The softest direction is along the
205 c-axis.

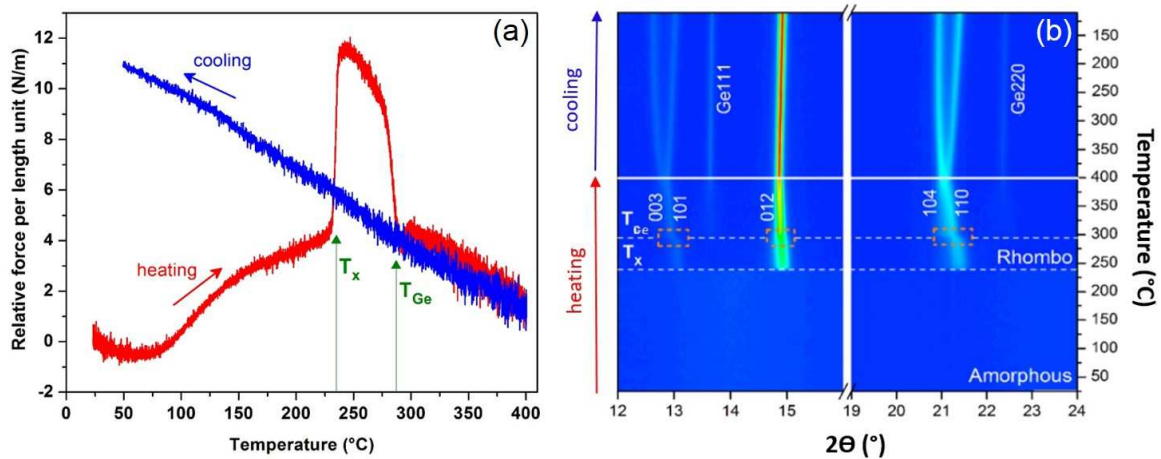
206 For the sake of completeness, it is worth mentioning the description of α GeTe with a pseudo-cubic
207 unit cell, since the rhombohedral cell is very close to a cubic NaCl one, stretched along the $\langle 111 \rangle$
208 direction. The α - β transition may be then viewed as a pseudo-cubic to cubic transition. In that case
209 the a_c parameter corresponds to the (111) interplanar distance of the primitive rhombohedral cell,
210 which leads to $a_c = 0.589$ to 0.599 nm and $\alpha_c = 88.35$ to 88.96° (instead of 90° in a cube).

211

212 4. Experimental results

213 Figure 2 shows the substrate curvature and XRD results obtained simultaneously *in situ* during
214 annealing of a 100 nm GeTe film up to 400°C . On the right-hand side, XRD patterns ($E = 16 \text{ keV}$) are
215 shown as a function of temperature. The area detector was placed such that it covers in a single image
216 a 2θ angular opening of about 5° ; thus, two detector positions have been used yielding two 2θ ranges,
217 from 12° to 16° and from 19° to 24° respectively. Starting from room temperature no diffraction peaks
218 are visible, which is in agreement with the expected amorphous nature of as-deposited films. From

219 239°C on distinct diffraction peaks appear, that can be assigned to rhombohedral α GeTe. They are
 220 indexed accordingly (in the hexagonal description, see above) as 003/101, 012, and 104/110. This
 221 temperature is thus the crystallization temperature of GeTe noted T_x from now on. The value of $T_x =$
 222 239°C is in good agreement with the literature for non-oxidized GeTe film[46]. Further heating makes
 223 faint additional peaks to appear at 297°C. These two additional peaks can be assigned to cubic Ge
 224 (diamond structure) and indexed as 111Ge and 220Ge. This temperature will be noted T_{Ge} from now
 225 on. In this combined experiment, $T_{Ge} \approx T_x + 58^\circ\text{C}$, and $T_{Ge}/T_x \approx 1.25$. A clear displacement of α GeTe
 226 diffraction peaks is evidenced at T_{Ge} . Upon cooling no additional peaks appear but splitting of α GeTe
 227 003/101 and 104/110 peaks is evidenced.



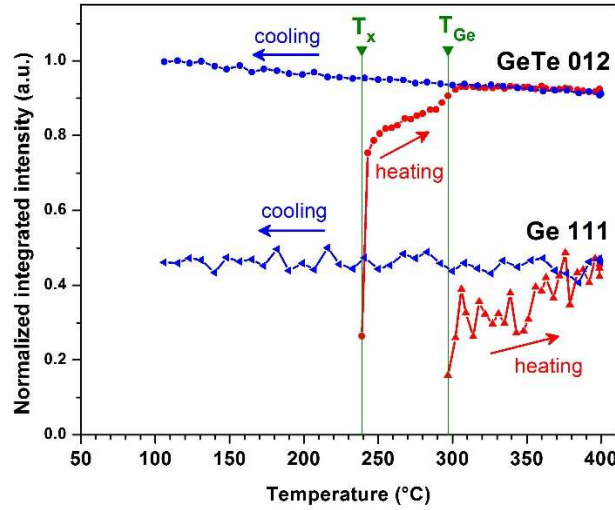
228
 229 *Figure 2* : In situ coupled measurements during the annealing of 100 nm GeTe films at $2^\circ\text{C}/\text{min}$. (a) Relative
 230 force deduced from substrate curvature; (b) XRD patterns ($E=16\text{ keV}$) as a function of temperature.

231
 232 The force deduced from the sample curvature (equation 2) is plotted against temperature in the left-
 233 hand side of figure 2. Upon annealing, after a first compressive evolution up to 70°C , a smooth tensile
 234 stress buildup is then observed until $T_x = 239^\circ\text{C}$ where a sharp tensile increase happens. Further
 235 heating yields a smooth compressive trend followed by a sharp compressive drop at $T_{Ge} = 297^\circ\text{C}$ and a
 236 linear compressive trend. Cooling down translates into a linear tensile evolution. From the nominal
 237 100 nm film thickness, one can deduce the stress jumps at T_x and T_{Ge} : $+72$ and -54 MPa respectively.
 238 These values are extracted assuming a constant thickness.

239 The diffraction peaks have been fitted using a Gaussian function and a linear background using a
 240 home-made python code. This allows extracting as a function of temperature the following
 241 parameters: peak integrated intensity, peak position and thus lattice spacing and peak width (FWHM).

242 The integrated intensity of α GeTe 012 and Ge 111 peaks is shown as a function of temperature in
 243 figure 3. At T_x a sharp increase of the 012 GeTe intensity is the signature of crystallization followed
 244 by a slow increase and a step at T_{Ge} . Upon cooling the intensity is almost constant with a slight
 245 increase that might be related to the Debye-Waller factor. The Ge 111 peak appears at T_{Ge} and steadily
 246 increases in intensity especially above 345°C (at $\sim T_{Ge} + 50^\circ\text{C}$, or $\sim 1.25T_{Ge}$). The decreasing evolution
 247 of the integrated intensity of α GeTe 012 after T_{Ge} and upon cooling may be explained by the
 248 beginning of the GeTe rhombohedral-cubic phase transition (already shown to begin around

249 350°C[24]) for high temperatures and by the Debye-Waller effect for the lowest temperatures.
 250 However the indexation reported in Figures 2, 3 and 4 correspond to the hexagonal description of the
 251 rhomboedral α -GeTe phase. The characteristic splitting of the 003/101 and 104/110 peaks upon
 252 cooling is a fingerprint for this phase. Upon heating the breadth of the Bragg peaks does not allow for
 253 resolving these splittings but there are no signs for α - β phase transition, which should show up e.g. in
 254 the evolution of the peak widths.



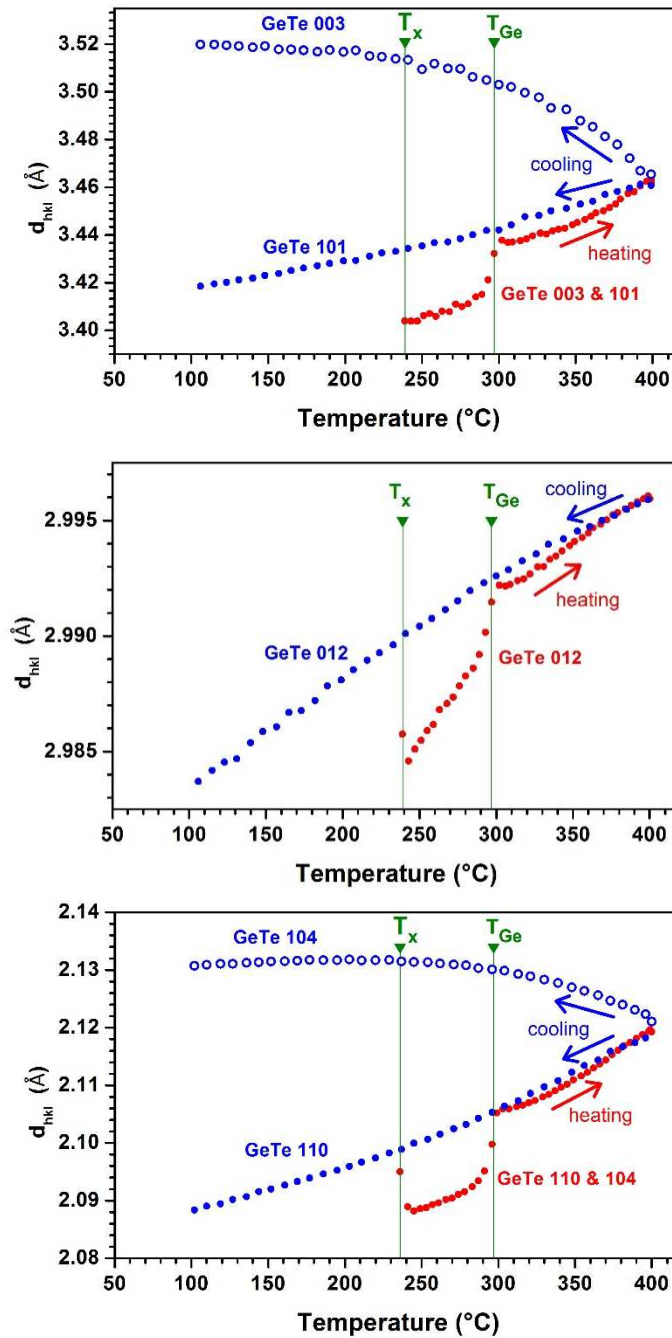
255
 256 *Figure 3* : Normalized integrated diffracted intensity of α GeTe 012 peak and Ge 111 peak. The normalization of
 257 the Ge 111 peak has been set to 0.5 for clarity. Its experimental integrated intensity is about 5 times smaller
 258 compared to GeTe 012.

259
 260 Lattice spacings deduced from the peak positions are shown in figure 4. Above T_x , all spacings exhibit
 261 a positive thermal expansion behavior with a monotonous increase when the temperature rises. At T_{Ge} ,
 262 a very distinct step is observed for all the measured spacings. Above T_{Ge} , positive thermal expansion
 263 resumes. Upon cooling specific splittings (003/101, 104/110) are observed with some peaks exhibiting
 264 negative thermal expansion in agreement with the reported thermal expansion coefficients[40–43].
 265 Table 1 shows the calculated (eq.(6)) and measured values of thermal expansion coefficients α_{hkl} for
 266 the main (hkl) lattice planes of α GeTe phase: lattice planes having very close interplanar distances
 267 (*i.e.* 003/101, and 104/110) exhibit opposite thermal expansion coefficients, and the measured α_{hkl} are
 268 in very good agreement with the calculated ones, which implies very small thermoelastic strains in
 269 these supported films.

270

(hkl)	d_{hkl} (nm)	calculated α_{hkl} (K ⁻¹) from eq.(6)	measured α_{hkl} (K ⁻¹) from Fig.4
(003)	0.355 ± 0.002	-2.05×10^{-5}	-1.78×10^{-5}
(101)	0.342 ± 0.001	$+2.65 \times 10^{-5}$	$+3.26 \times 10^{-5}$
(012)	0.2988 ± 0.0005	$+1.53 \times 10^{-5}$	$+1.46 \times 10^{-5}$
(104)	0.2144 ± 0.0005	-0.22×10^{-5}	-0.14×10^{-5}
(110)	0.2084 ± 0.0005	$+3.19 \times 10^{-5}$	$+3.77 \times 10^{-5}$

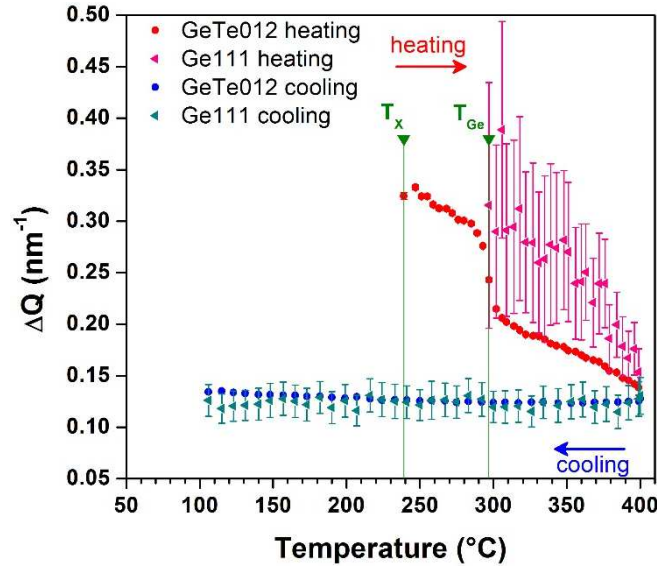
271 *Table 1: Temperature interplanar distances (at room temperature) and thermal expansion coefficients α_{hkl} for*
 272 *the main diffraction lines of α GeTe: theoretical α_{hkl} is calculated from eq. (6) and the lattice parameters from*
 273 *Ref.39 ; the measured α_{hkl} is calculated from the d_{hkl} of figure 4, during cooling, between 100°C and 300°C.*



274
 275 *Figure 4: Lattice spacings in the α GeTe film as a function of temperature extracted from peak fitting of figure 2.*
 276

277 The thermal evolution of α GeTe 012 and Ge 111 FWHMs is shown in figure 5. Note that under
 278 experimental conditions, the experimental resolution on DiffAbs beamline is in the range of [0.04°-
 279 0.09°] in 2θ (and varying linearly with respect to the 2θ position of the XRD peak), leading to an
 280 experimental resolution around $2\theta = 15^\circ$ in reciprocal space units in the range of 0.07 nm^{-1} , thus

281 negligible in figure 5. The width of α GeTe 012 peak is decreasing with temperature with a sharp step
 282 down at T_{Ge} . Upon cooling this width stays constant. The width of Ge 111 peak decreases with
 283 annealing temperature and stays constant during the cooling stage.

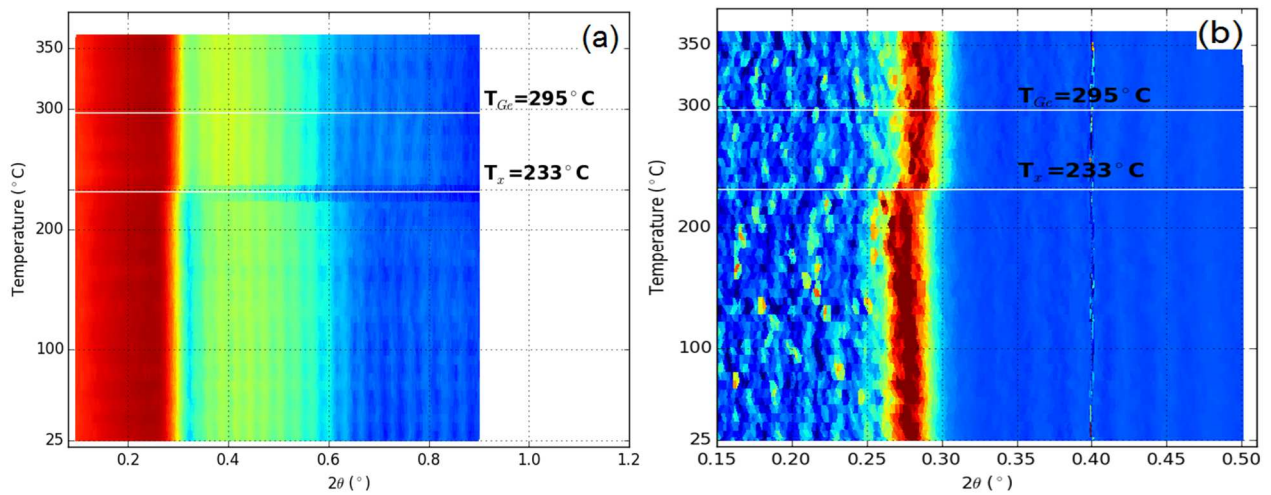


284

285 *Figure 5: Diffraction peak widths of α GeTe 012 and Ge 111 as a function of temperature in reciprocal space*
 286 *units.*

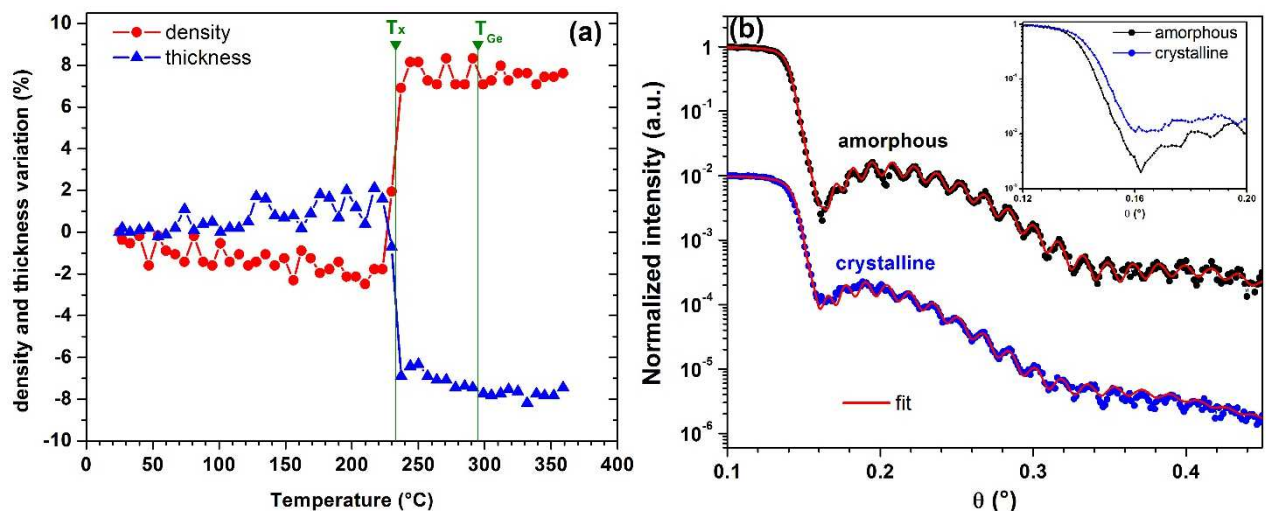
287

288 In-situ XRR patterns and total reflection edge (θ_c) variations are shown in figure 6 according to
 289 temperature. Starting from room temperature, the XRR patterns (total reflection edge θ_c and Kiessig
 290 fringes position) remain almost constant up to T_x where a clear shift in θ_c occurs towards higher angle
 291 (see figure 6b), corresponding to an increase in mass density. A second slight irregularity happens at
 292 T_{Ge} . During the heating stage, each XRR pattern was fitted to extract both the mass density and the
 293 film thickness change (see figure 7a). Figure 7b shows two XRR patterns recorded at the beginning of
 294 annealing (amorphous) and after T_x (crystallized), the corresponding fits, and a zoom on the total
 295 reflection edge indicating the shift through higher angle for the crystallized sample. Starting from a
 296 density of $(5.64 \pm 0.01) \text{ g.cm}^{-3}$ and a film thickness of $(98.8 \pm 0.1) \text{ nm}$, these values show respectively
 297 an average decrease and increase of -2.2% and $+1.9 \%$ even before reaching T_x . The average value
 298 of $+2\%$ in the thickness variation up to T_x corresponds to a linear thermal expansion coefficient of
 299 $\sim 2.2 \times 10^{-5} \text{ K}^{-1}$, in good agreement with the average value of $\alpha_v/3$ reported in literature for crystalline
 300 GeTe [40–43]. Around T_x , the mass density and film thickness show respectively a relative variation
 301 of about $+8 \%$ and -7% , then the mass density remains almost constant and the film thickness still
 302 changes to reach $\sim 8 \%$ at the end of annealing. From these data, the mass density of the GeTe film is
 303 calculated at 5.64 g/cm^3 and 6.07 g/cm^3 in respectively the amorphous and crystallized phases,
 304 corresponding to a relative variation of $+7.6 \%$, in agreement with literature[39].



305

306 *Figure 6: In situ combined XRR measurement ($E = 18$ keV) on 100 nm GeTe annealed at $2^\circ\text{C}/\text{min}$: (a) in situ*
 307 *XRR patterns; (b) Variation of the total reflection edge θ_c according to temperature (extracted from the*
 308 *derivative of XRR patterns).*



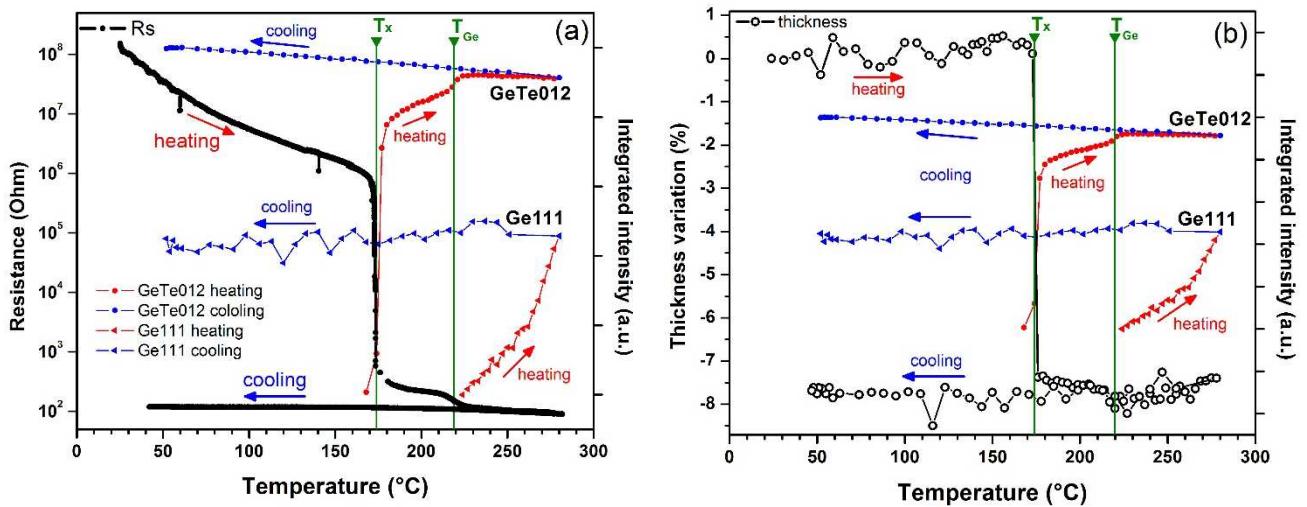
309

310 *Figure 7: (a) Density and thickness relative variation extracted from the fit of in situ XRR patterns and (b) XRR*
 311 *experimental and fitted patterns recorded during annealing; as an example, 2 datasets are shown: at the*
 312 *beginning (amorphous sample) and at $T = 339^\circ\text{C}$ (crystalline sample).*

313

314 Finally, to correlate the structural and electrical properties of the layer upon crystallization, combined
 315 XRD, XRR and R_s were performed. Figure 8a shows the evolution of R_s and XRD integrated intensity
 316 of αGeTe 012 and Ge 111 peaks with temperature upon *in situ* annealing up to 300°C and subsequent
 317 cooling. One should note that because of the sample holder pressing the sample on one side against the
 318 heating element, and because of the different thermal conditions compared to previous experiments
 319 (under vacuum vs. nitrogen atmosphere annealing), both T_x and T_{Ge} are shifted to lower temperatures;
 320 however, the data does not evidence any oxidation process responsible of such a shift[46], only the

321 different thermal conditions are involved. Apart from this shift in temperature, the XRD integrated
 322 intensity evolution shown in figure 8a are similar to the ones obtained in figures 2b and 3: actually, (i)
 323 the α GeTe 012 Bragg reflection shows a clear 2 step-growth (sharp increase at T_x followed by a slow
 324 increase and a step at T_{Ge} , with $T_{Ge} \approx T_x + 45^\circ\text{C}$ and $T_{Ge}/T_x \approx 1.25$) and the same shift in 2θ position at
 325 T_{Ge} ; and (ii) the Ge111 peaks displays a steady increase in intensity above 265°C (at $\sim T_{Ge} + 45^\circ\text{C}$ or
 326 $\sim 1.2T_{Ge}$). The sheet resistance evolution with temperature shows that the sample is initially in a highly
 327 resistive amorphous state, and, up to T_x , the resistance decreases with temperature as expected for a
 328 typical semiconductor. At T_x , the resistance drops suddenly by several orders of magnitude. A second
 329 drop of R_s occurs at T_{Ge} , then low resistance state is conserved upon cooling. Taking into account the
 330 film thickness at RT before and after crystallization, the resistivity is $\rho_a = 1.6 \times 10^3 \Omega\cdot\text{cm}$ and $\rho_c = 1.05$
 331 $\text{m}\Omega\cdot\text{cm}$, respectively in the amorphous and crystallized layer. The electrical contrast, defined as
 332 $\Delta R_s = \frac{R_{S\text{ before}}}{R_{S\text{ after}}}$, is 1.4×10^6 . These values are all consistent with literature[47]. Both XRR (film
 333 thickness evolution) and XRD (GeTe 012 and Ge 111 integrated intensities) results are compared in
 334 figure 8b: the relative thickness variation is $\sim 0.4\%$ before T_x (the corresponding linear thermal
 335 expansion coefficient is $\sim 2.6 \cdot 10^{-5} \text{ K}^{-1}$, thus in the same order of magnitude as in figure 7a), then a
 336 drastic decrease of -7.5% occurs at T_x . At T_{Ge} a limited irregularity in the thickness evolution is
 337 visible. The relative variation of thickness after/before annealing is -7.7% , also in good accordance
 338 with previous results obtained with combined XRD and XRR only.



339
 340 *Figure 8: Results of combined XRD, XRR and R_s experiment on 100 nm GeTe layer capped with 10nm SiN. (a)*
 341 *R_s (left scale) and normalized integrated diffracted intensity (right scale) of α GeTe 012 peak and Ge 111 peak.*
 342 *The normalization of Ge 111 peak has been set to 0.5 for clarity. Its experimental integrated intensity is about 5*
 343 *times smaller compared to GeTe 012. (b) relative layer thickness variation (left scale) deduced from XRR*
 344 *patterns and normalized integrated diffracted intensity (right scale) of α GeTe 012 peak and Ge 111 peak.*

345
 346 **5. Discussion**

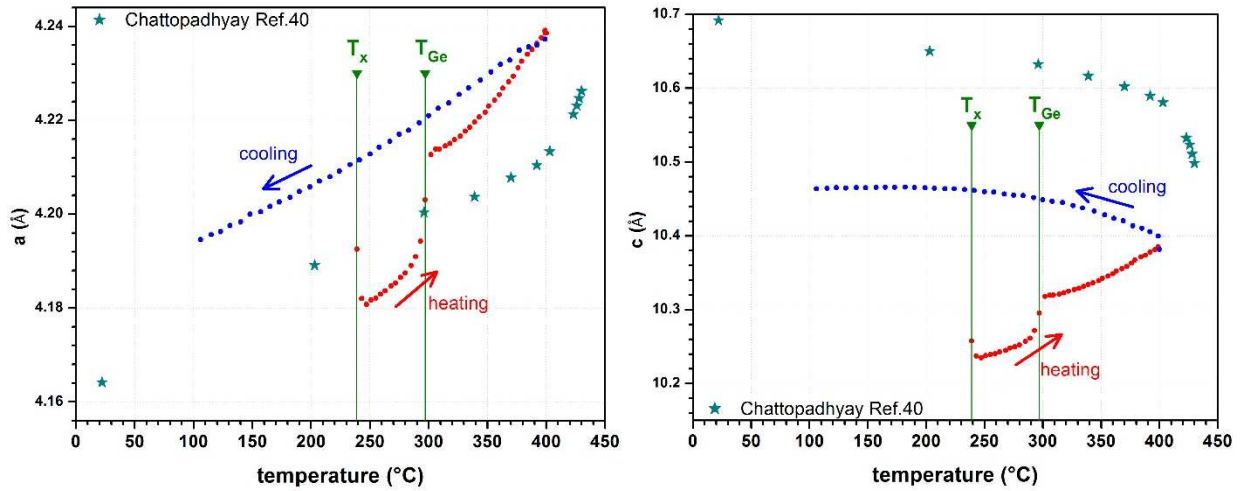
347 The *in situ* evolutions during the annealing of the capped 100 nm GeTe films described in the previous
348 section can be summarized in the following way:

- 349 • Stage I RT- T_x : Between room temperature and $T_x = 239^\circ\text{C}$ the film stays amorphous (no XRD
350 peak), with a high electrical resistance state, and a tensile stress evolution is observed. During
351 this stage a decrease of $\sim -2.2\%$ in mass density is measured by XRR, indicating that the
352 tensile stress buildup is not related to a layer densification but rather to structural re-
353 arrangements occurring in the amorphous GeTe phase during heating.
- 354 • Stage II T_x - T_{Ge} : at $T_x = 239^\circ\text{C}$ an abrupt tensile stress jump is observed (+72 MPa) followed by
355 a slight compressive stress evolution. αGeTe diffraction peaks appear at T_x as a consequence
356 of crystallization. X-ray reflectivity indicates a densification of the film (+8%) and a
357 decrease of the film thickness (-7%). The electrical resistivity shows a decrease of several
358 orders of magnitude.
- 359 • Stage III T_{Ge} - T_{max} : at $T_{\text{Ge}} = 297^\circ\text{C}$ diffraction peaks from Ge appear. At the same time distinct
360 steps are observed in: (i) stress (compressive jump -54 MPa); (ii) αGeTe lattice spacings; (iii)
361 αGeTe peak widths; (iv) αGeTe integrated intensity; (v) electrical resistivity (second
362 decrease).
- 363 • Upon cooling the film stays crystallized. Both αGeTe and Ge diffraction peaks are present
364 and exhibit a thermoelastic behavior.

365 Before focusing on stage III which shows the most novel results, a few points deserve to be
366 highlighted concerning Stage II and crystallization. The crystallization temperature of our 100 nm
367 thick GeTe films is 239°C , which shows that surface oxidation has been effectively prevented[46].
368 Crystallization is shown to be associated with an important increase in density together with a tensile
369 stress buildup, in agreement with literature[48]. It is worth noting that such a density change should
370 yield stresses of the order of several GPa if one takes into account the elastic constants of
371 GeTe[44,45]. Although we do measure tensile stresses, in qualitative agreement with a densification,
372 they are two orders of magnitude smaller than the ones predicted from elasticity. This shows that a
373 very important relaxation of stresses occurs during crystallization, probably by viscous flow in the
374 amorphous phase as already proposed in the literature[49].

375 Let us now discuss the interesting phenomena occurring upon Ge crystallization. In agreement with
376 the initial film composition and with the equilibrium phase diagram[37], pure Ge precipitates within
377 the film at T_{Ge} . Above T_{Ge} the decrease of the Ge111 peak width (Fig. 5) can be interpreted as an
378 increase of the Ge grain size up to about 40 nm. The Ge 111 integrated intensity (Fig. 3 and 8), which
379 is proportional to the amount of crystallized material in the absence of texture evolution, increases
380 continuously as a function of temperature. Hence we observe both an increase in the quantity of
381 crystallized Ge and an increase in grain size. *Post mortem* observations by atom probe tomography
382 have recently evidenced large Ge grains in an annealed GeTe film[50]. As it is discussed in the
383 introduction, excess Ge precipitation is rather common in thin chalcogenide films and has been
384 described in several articles[18–23]. What has not been reported before are the consequences of this
385 precipitation on the αGeTe phase. At T_{Ge} , a rather sharp increase in the GeTe lattice spacings is
386 observed. From these spacings the average hexagonal lattice parameters are calculated and shown in

387 figure 9. Both a and c lattice parameters increase sharply at T_{Ge} , which translate in a 1.5 % increase in
 388 the volume of the unit cell. This volume increase agrees qualitatively with the compressive stress
 389 evolution evidenced by curvature measurements at T_{Ge} . Upon cooling one observes a negative thermal
 390 expansion coefficient along c, in agreement with literature[43]. Upon heating, the observed positive
 391 thermal expansion coefficient along c is probably related to the fact that both 003 and 101 diffraction
 392 lines, and 110 and 104 diffraction lines, are not resolved by the XRD measurement to be fitted
 393 separately, implying that only an average of the lattice spacings can be measured upon heating.



394 *Figure 9: Lattice parameters of α GeTe as a function of temperature. Results from the literature on bulk samples*
 395 *[Ref.40] are also shown.*

396
 397 The width of the GeTe diffraction peaks (Fig. 5) shows a sharp drop at T_{Ge} . Although peak width
 398 is related to crystallite size (but not only), it is difficult to believe that GeTe grain size increases by
 399 25% at T_{Ge} (Fig. 5). This drop is more likely caused by a sudden reduction of the dispersion in
 400 lattice spacing (inter grains or intra-grains). Such an effect is called microstrain in the line-profile-
 401 analysis community[51] and causes a peak broadening that is proportional to the distance to the
 402 origin of reciprocal space (whereas size broadening is independent on the position in reciprocal
 403 space). Without going to a very involved line profile analysis that is out of the scope of this study
 404 one can use a simple Williamson-Hall analysis[52], which states that size and micro-deformation
 405 broadening are additive:

$$\Delta q = 2\pi/L + \varepsilon q$$

406
 407 where L is the crystal size, q the magnitude of the scattering vector and ε the microstrain, which is
 408 basically the standard deviation of the relative lattice spacing distribution. In the Williamson-Hall
 409 method one uses several orders of diffraction in order to plot Δq vs q and extract L and ε . Here we
 410 may assume that the step at T_{Ge} is purely caused by microstrains and that above T_{Ge} broadening is
 411 solely caused by size. Such a hypothesis yields: $\varepsilon = 5 \times 10^{-3}$, an initial grain size of 26 nm (before
 412 T_{Ge}) and a final grain size of 40 nm (at T_{max}).

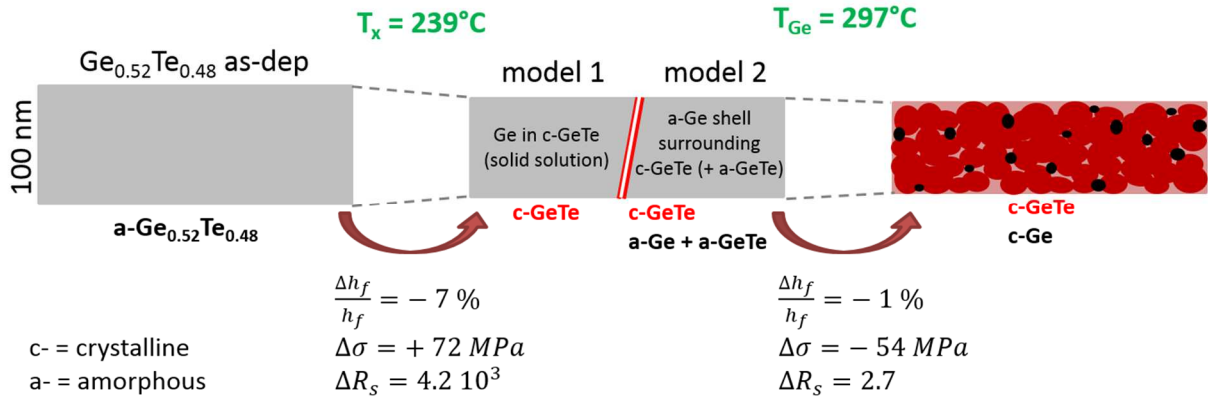
413 Finally, one may wonder about the state of Ge between T_x and T_{Ge} , *i.e.* when GeTe is crystallized
 414 and before the appearance of crystallized Ge. One may consider two extreme possibilities: 1) Ge is

415 in solution in αGeTe ; 2) or Ge is an amorphous state. This makes two possible models for
416 explaining our experimental findings.

417 • Model 1: Ge is in solid solution in αGeTe . At T_x , αGeTe crystallizes and excess Ge is
418 within the unit cell in interstitial sites. At T_{Ge} , Ge becomes mobile and can precipitate out
419 of the Ge-rich phase. In this interpretation, the volume of the unit cell needs to decrease
420 upon Ge rejection. This decrease in volume in the supported film implies a compressive
421 stress as observed experimentally. The increase of GeTe lattice parameters upon Ge
422 rejection does not, however, agree with what has been published on the dependence of
423 GeTe unit cell with composition: Hohnke[53] reports that the unit cell volume of Ge-
424 saturated GeTe is larger than the one of Te-saturated GeTe. Diffracted intensity increase
425 and resistivity decrease are related to the change in structure factor and doping
426 respectively. The decrease in microstrain may be caused by an inhomogeneity in Ge
427 excess concentration between grains below T_{Ge} that disappears when Ge is rejected
428 leading to stable αGeTe .

429
430 • Model 2: An amorphous Ge shell is surrounding the αGeTe grains, with still small
431 amorphous GeTe domains. It is actually worth noting that EXAFS analyses from
432 Kolobov[54] seems to indicate the presence of amorphous Ge coexisting with crystallized
433 GeTe. At T_x excess Ge is rejected in the form of a thin amorphous shell that surrounds the
434 αGeTe grains and put them under compression. At T_{Ge} , Ge crystallizes in the form of
435 localized grains thus relieving the applied stress, and leading to an increase in the GeTe
436 unit cell volume. The remaining amorphous GeTe domains, having probably a Ge-rich
437 composition, crystallize at the same temperature T_{Ge} , which is higher than T_x for
438 stoichiometric GeTe, as already shown[24]. Diffracted intensity increase and resistivity
439 decrease at T_{Ge} are related to the crystallization of remaining GeTe and/or to removal of
440 amorphous Ge at GeTe grain boundaries that can be responsible for electronic localization
441 effect and hindering thus electronic transport. The bulk modulus of αGeTe is of the order
442 of 50 GPa hence the hydrostatic stress corresponding to 1.5% volume change is 750 MPa.
443 This positive relief of internal strain in a supported film yields a compressive stress
444 buildup, as observed. The disappearance of microstrains may be understood as a
445 homogenization of the elastic strains in the film. Indeed at T_{Ge} the GeTe grains are not
446 strained anymore by the amorphous Ge shell whereas below T_{Ge} elastic strains will vary
447 from one grain to the other depending on the size and orientation of the grains as well as
448 on the thickness of the shell. Moreover the disappearance of the amorphous Ge shell is
449 likely to be responsible for the lowering of electrical resistance.

450 These two models are schematized in figure 10.



451 *Figure 10: Schematic illustration of the two possible models. h_f is the layer thickness, σ is the stress, ΔR_s is the*
 452 *electrical contrast.*

453

454 6. Conclusion

455 Original combinations of x-ray diffraction and x-ray reflectivity with curvature or resistance
 456 measurements have been performed *in situ* during annealing of initially amorphous GeTe thin films on
 457 silicon at DiffAbs beamline at SOLEIL synchrotron facility. These detailed experiments reveal a
 458 complex behavior with successive structural changes such as rhombohedral GeTe crystallization or
 459 cubic Ge precipitation accompanied by abrupt stress and resistance changes. In particular, this study
 460 reveals that crystalline Ge precipitation results in important changes (volume of the unit cell,
 461 homogeneity of lattice spacing, average stress, ...) in the surrounding GeTe matrix. Different
 462 scenarios are proposed to understand these results. Future works at the local scale (atom probe
 463 tomography, transmission electron microscopy) will certainly help in selecting which scenario is at
 464 work. Based on our results we suggest, however, that the formation of an amorphous Ge shell around
 465 GeTe grains is the most probable event. Beyond its fundamental interest, this complex interplay
 466 between stress and composition in GeTe thin films has important implications for PCRAM
 467 technology. Indeed phase change materials used in Non-Volatile Memories are often strongly off-
 468 stoichiometric and Ge rejection and crystallization play a key role in the functioning of these devices.

469

470 ACKNOWLEDGMENTS

471 This work has been funded by ANR under contract SESAME ANR-15-CE24-0021. We would like to
 472 thank SOLEIL synchrotron for allocating beamtime on DiffAbs beamline.

473 Ph. Joly (Synchrotron SOLEIL, DiffAbs) is thanked for technical support.

474

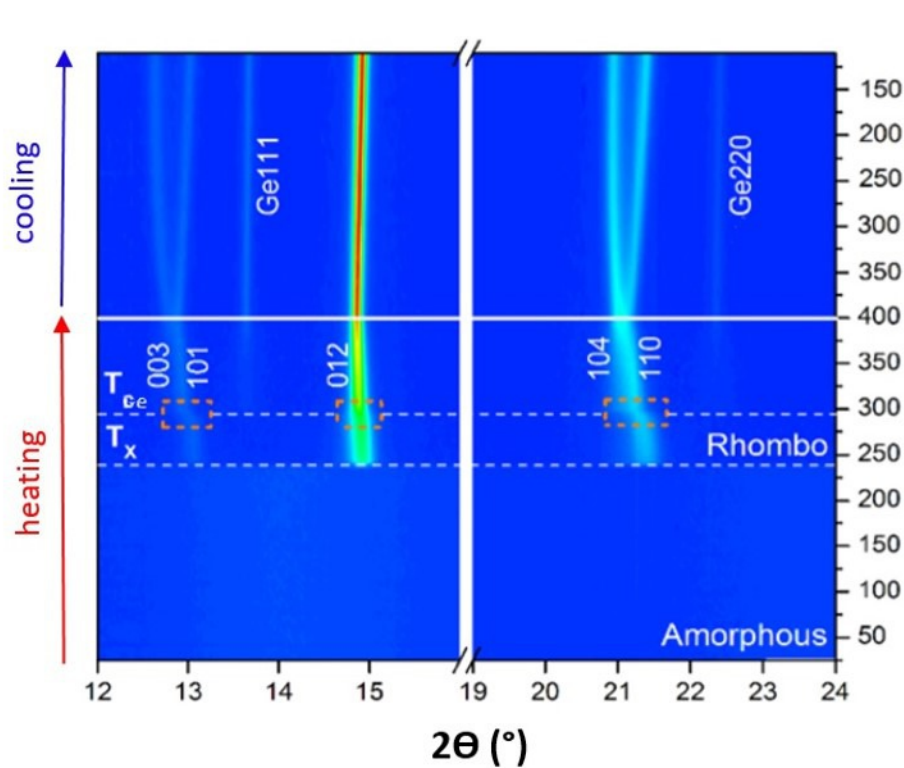
475 **REFERENCES**

- 476 [1] V.L. Deringer, R. Dronskowski, M. Wuttig, Microscopic Complexity in Phase-Change
477 Materials and its Role for Applications, *Adv. Funct. Mater.* 25 (2015) 6343–6359.
478 doi:10.1002/adfm.201500826.
- 479 [2] G.W. Burr, M.J. BrightSky, A. Sebastian, H.-Y. Cheng, J.-Y. Wu, S. Kim, N.E. Sosa, N.
480 Papandreou, H.-L. Lung, H. Pozidis, E. Eleftheriou, C.H. Lam, Recent Progress in Phase-
481 Change Memory Technology, *IEEE J. Emerg. Sel. Top. Circuits Syst.* 6 (2016) 146–162.
482 doi:10.1109/JETCAS.2016.2547718.
- 483 [3] P. Noé, C. Vallée, F. Hippert, F. Fillot, J.-Y. Raty, Phase-change materials for non-volatile
484 memory devices: from technological challenges to materials science issues, *Semicond. Sci.*
485 *Technol.* 33 (2018) 13002. doi:10.1088/1361-6641/aa7c25.
- 486 [4] A. Caretta, B. Casarin, P. Di Pietro, A. Perucchi, S. Lupi, V. Bragaglia, R. Calarco, F.R.L.
487 Lange, M. Wuttig, F. Parmigiani, M. Malvestuto, Interband characterization and electronic
488 transport control of nanoscaled GeTe/Sb₂Te₃ superlattices, *Phys. Rev. B.* 94 (2016) 045319.
489 doi:10.1103/PhysRevB.94.045319.
- 490 [5] J.-J. Wang, Y.-Z. Xu, R. Mazzarello, M. Wuttig, W. Zhang, A Review on Disorder-Driven
491 Metal–Insulator Transition in Crystalline Vacancy-Rich GeSbTe Phase-Change Materials,
492 *Materials (Basel).* 10 (2017) 862. doi:10.3390/ma10080862.
- 493 [6] J.E. Boschker, R. Wang, R. Calarco, GeTe: A simple compound blessed with a plethora of
494 properties, *CrystEngComm.* 19 (2017) 5324–5335. doi:10.1039/c7ce01040k.
- 495 [7] J.Y. Raty, W. Zhang, J. Luckas, C. Chen, R. Mazzarello, C. Bichara, M. Wuttig, Aging
496 mechanisms in amorphous phase-change materials, *Nat. Commun.* 6 (2015) 1–8.
497 doi:10.1038/ncomms8467.
- 498 [8] J. Raty, M. Schumacher, P. Golub, V.L. Deringer, C. Gatti, M. Wuttig, A Quantum-Mechanical
499 Map for Bonding and Properties in Solids, *Adv. Mater.* 31 (2019) 1806280.
500 doi:10.1002/adma.201806280.
- 501 [9] M. Wuttig, S. Raoux, *The Science and Technology of Phase Change Materials*, *Zeitschrift Für*
502 *Anorg. Und Allg. Chemie.* 638 (2012) 2455–2465. doi:10.1002/zaac.201200448.
- 503 [10] M. Putero, T. Ouled-Khachroum, M.-V. Coulet, D. Deleruyelle, E. Ziegler, C. Muller,
504 Evidence for correlated structural and electrical changes in a Ge₂Sb₂Te₅ thin film from
505 combined synchrotron X-ray techniques and sheet resistance measurements during in situ
506 thermal annealing, *J. Appl. Crystallogr.* 44 (2011) 858–864. doi:10.1107/S0021889811024095.
- 507 [11] N. Yamada, E. Ohno, N. Akahira, K. Nishiuchi, K. Nagata, M. Takao, High speed overwritable
508 phase change optical disk material, *Jpn. J. Appl. Phys.* 26 (1987) 61–66.
- 509 [12] H.-Y. Cheng, J. Wu, R. Cheek, S. Raoux, M. BrightSky, D. Garbin, S. Kim, T. Hsu, Y. Zhu, E.
510 Lai, E. Joseph, A. Schrott, S. Lai, A. Ray, H. Lung, C. Lam, A thermally robust phase change
511 memory by engineering the Ge/N concentration in (Ge, N)_xSb_yTe_z phase change material,
512 in: *IEDM Tech. Dig. IEEE Int. Electron Devices Meet.*, 2012: pp. 31.1.1-31.1.4.
513 doi:10.1109/IEDM.2012.6479141.
- 514 [13] A. Kiouseloglou, G. Navarro, V. Sousa, A. Persico, A. Roule, A. Cabrini, G. Torelli, S.
515 Maitrejean, G. Reimbold, B. De Salvo, F. Clermidy, L. Perniola, A Novel Programming
516 Technique to Boost Low-Resistance State Performance in Ge-Rich GST Phase Change
517 Memory, *IEEE Trans. Electron Devices.* 61 (2014) 1246–1254.
- 518 [14] M. Chen, K.A. Rubin, R.W. Barton, Compound materials for reversible, phase-change optical
519 data storage, *Appl. Phys. Lett.* 49 (1986) 502–504. doi:10.1063/1.97617.
- 520 [15] S. Yoon, K. Choi, N. Lee, S. Lee, Y. Park, B. Yu, Nanoscale observations of the operational
521 failure for phase-change-type nonvolatile memory devices using Ge₂Sb₂Te₅ chalcogenide thin
522 films, *Appl. Surf. Sci.* 254 (2007) 316–320. doi:10.1016/j.apsusc.2007.07.098.
- 523 [16] G. Navarro, V. Sousa, a. Persico, N. Pashkov, a. Toffoli, J.-C. Bastien, L. Perniola, S.
524 Maitrejean, a. Roule, P. Zuliani, R. Annunziata, B. De Salvo, Material engineering of

- 525 GexTe100-x compounds to improve phase-change memory performances, *Solid. State.*
526 *Electron.* 89 (2013) 93–100. doi:10.1016/j.sse.2013.07.005.
- 527 [17] S. Raoux, C. Cabral, L. Krusin-Elbaum, J.L. Jordan-Sweet, K. Virwani, M. Hitzbleck, M.
528 Salinga, A. Madan, T.L. Pinto, Phase transitions in Ge–Sb phase change materials, *J. Appl.*
529 *Phys.* 105 (2009) 064918. doi:10.1063/1.3091271.
- 530 [18] L. Krusin-Elbaum, D. Shakhvorostov, C. Cabral, S. Raoux, J.L. Jordan-Sweet, Irreversible
531 altering of crystalline phase of phase-change Ge–Sb thin films, *Appl. Phys. Lett.* 96 (2010)
532 121906. doi:10.1063/1.3361656.
- 533 [19] G.B. Kim, J.H. Bae, S.M. Jeong, S.M. Choi, H.L. Lee, Crystallization properties of Ge1-xSbx
534 thin films ($x = 0.58-0.88$, *Jpn. J. Appl. Phys.* 50 (2011). doi:10.1143/JJAP.50.045805.
- 535 [20] P. Zalden, G. Aquilanti, C. Prestipino, O. Mathon, B. André, M. Wuttig, M.V. Coulet,
536 Simultaneous calorimetric and quick-EXAFS measurements to study the crystallization process
537 in phase-change materials., *J. Synchrotron Radiat.* 19 (2012) 806–13.
538 doi:10.1107/S090904951202612X.
- 539 [21] M. Putero, M.-V. Coulet, C. Muller, C. Baethz, S. Raoux, H.-Y. Cheng, Ge-doped GaSb thin
540 films with zero mass density change upon crystallization for applications in phase change
541 memories, *Appl. Phys. Lett.* 108 (2016) 101909. doi:10.1063/1.4943788.
- 542 [22] S.M.S. Privitera, V. Sousa, C. Bongiorno, G. Navarro, C. Sabbione, E. Carria, E. Rimini,
543 Atomic diffusion in laser irradiated Ge rich GeSbTe thin films for phase change memory
544 applications, *J. Phys. D. Appl. Phys.* 51 (2018). doi:10.1088/1361-6463/aab1d0.
- 545 [23] E. Gourvest, S. Lhostis, J. Kreisel, M. Armand, S. Maitrejean, A. Roule, C. Vallé, Evidence of
546 Germanium precipitation in phase-change Ge1-xTexthin films by Raman scattering, *Appl.*
547 *Phys. Lett.* 95 (2009) 4–6. doi:10.1063/1.3186077.
- 548 [24] S. Raoux, B. Muñoz, H.-Y. Cheng, J.L. Jordan-Sweet, Phase transitions in Ge–Te phase
549 change materials studied by time-resolved x-ray diffraction, *Appl. Phys. Lett.* 95 (2009)
550 143118. doi:10.1063/1.3236786.
- 551 [25] W. Knaepen, S. Gaudet, C. Detavernier, R.L. Van Meirhaeghe, J. Jordan-Sweet, C. Lavoie, In
552 situ x-ray diffraction study of metal induced crystallization of amorphous germanium, *J. Appl.*
553 *Phys.* 105 (2009) 83532. doi:10.1063/1.3110722.
- 554 [26] J.M. del Pozo, M.P. Herrero, L. Díaz, Crystallization behaviour of amorphous Ge(1 - x)Sb_xthin
555 films, *J. Non. Cryst. Solids.* 185 (1995) 183–190. doi:10.1016/0022-3093(95)00663-X.
- 556 [27] X. Yi, Z. Wang, F. Dong, S. Cheng, J. Wang, C. Liu, J. Li, S. Wang, T. Yang, W.S. Su, L.
557 Chen, Structural and optical properties of Ge60Te40: Experimental and theoretical verification,
558 *J. Phys. D. Appl. Phys.* 49 (2016) 155105. doi:10.1088/0022-3727/49/15/155105.
- 559 [28] E. Carria, A.M. Mio, S. Gibilisco, M. Miritello, C. Bongiorno, M.G. Grimaldi, E. Rimini,
560 Amorphous-Crystal Phase Transitions in GexTe1-x Alloys, *J. Electrochem. Soc.* 159 (2012)
561 H130. doi:10.1149/2.048202jes.
- 562 [29] T.O. Khachroum, M.-I. Richard, P. Noe, C. Guichet, C. Mocuta, C. Sabbione, F. Hippert, O.
563 Thomas, Stress buildup during crystallization of thin chalcogenide films for memory
564 applications: in situ combination of synchrotron X-Ray diffraction and wafer curvature
565 measurements, *Thin Solid Films.* 617 (2016) 44–47. doi:10.1016/j.tsf.2016.02.020.
- 566 [30] C. Mocuta, S. Stanescu, M. Gallard, A. Barbier, A. Dawiec, B. Kedjar, N. Leclercq, D.
567 Thiaudiere, Fast X-ray reflectivity measurements using an X-ray pixel area detector at the
568 DiffAbs beamline, Synchrotron SOLEIL, *J. Synchrotron Radiat.* 25 (2018) 204–213.
569 doi:10.1107/S1600577517015703.
- 570 [31] S. Basolo, J. Berar, N. Boudet, P. Breugnon, B. Caillot, J.-C. Clemens, P. Delpierre, B.
571 Dinkespiler, I. Koudobine, C. Meessen, M. Menouni, C. Mouget, P. Pangaud, R. Potheau, E.
572 Vigeolas, XPAD: Pixel detector for material sciences, 2005. doi:10.1109/TNS.2005.856818.
- 573 [32] P. Pangaud, S. Basolo, N. Boudet, J.F. Berar, B. Chantepie, J.C. Clemens, P. Delpierre, B.
574 Dinkespiler, K. Medjoubi, S. Hustache, M. Menouni, C. Morel, XPAD3-S: A fast hybrid pixel
575 readout chip for X-ray synchrotron facilities, *Nucl. Instruments Methods Phys. Res. Sect. A*

- 576 Accel. Spectrometers, Detect. Assoc. Equip. 591 (2008) 159–162.
577 doi:10.1016/j.nima.2008.03.047.
- 578 [33] C. Le Bourlot, P. Landois, S. Djaziri, P.O. Renault, E. Le Bourhis, P. Goudeau, M. Pinault, M.
579 Mayne-Lhermite, B. Bacroix, D. Faurie, O. Castelneau, P. Launois, S. Rouzire, Synchrotron X-
580 ray diffraction experiments with a prototype hybrid pixel detector, *J. Appl. Crystallogr.* 45
581 (2012) 38–47. doi:10.1107/S0021889811049107.
- 582 [34] C. Mocuta, M.I. Richard, J. Fouet, S. Stanescu, A. Barbier, C. Guichet, O. Thomas, S.
583 Hustache, A. V. Zozulya, D. Thiaudière, Erratum: Fast pole figure acquisition using area
584 detectors at the DiffAbs beamline - Synchrotron SOLEIL (*Journal of Applied Crystallography*
585 (2013) 46 (1842-1853)), *J. Appl. Crystallogr.* 47 (2014) 482.
586 doi:10.1107/S1600576713032081.
- 587 [35] C. Rivero, P. Gergaud, M. Gailhanou, O. Thomas, B. Froment, H. Jaouen, V. Carron,
588 Combined synchrotron x-ray diffraction and wafer curvature measurements during Ni–Si
589 reactive film formation, *Appl. Phys. Lett.* 87 (2005) 041904. doi:10.1063/1.1999021.
- 590 [36] M. Putero, B. Duployer, I. Blum, T. Ouled-Khachroum, M.-V. Coulet, C. Perrin, E. Ziegler, C.
591 Muller, D. Mangelinck, Combined in situ x-ray scattering and electrical measurements for
592 characterizing phase transformations in nanometric functional films, *Thin Solid Films.* 541
593 (2013) 21–27. doi:10.1016/j.tsf.2012.11.131.
- 594 [37] D.I. Bletskan, PHASE EQUILIBRIUM IN BINARY SYSTEMS A 1 vBv 1, *J. Ovonic Res. I*
595 (2005) 53–60.
- 596 [38] A. Onodera, I. Sakamoto, Y. Fujii, N. Môri, S. Sugai, Structural and electrical properties of
597 GeSe and GeTe at high pressure, *Phys. Rev. B.* 56 (1997) 7935–7941.
598 doi:10.1103/PhysRevB.56.7935.
- 599 [39] T. Nonaka, Crystal structure of GeTe and Ge₂Sb₂Te₅ meta-stable phase, *Thin Solid Films.* 370
600 (2000) 258–261. doi:10.1016/S0040-6090(99)01090-1.
- 601 [40] T. Chattopadhyay, J.X. Boucherle, H.G. von Schnering, Neutron diffraction study on the
602 structural phase transition in gete, *J. Phys. C Solid State Phys.* 20 (1987) 1431–1440.
603 doi:10.1088/0022-3719/20/10/012.
- 604 [41] T. Chatterji, C.M.N. Kumar, U.D. Wdowik, Anomalous temperature-induced volume
605 contraction in GeTe, *Phys. Rev. B.* 91 (2015) 054110. doi:10.1103/PhysRevB.91.054110.
- 606 [42] H. Wiedemeier, P.A. Siemers, The Thermal Expansion of GeS and GeTe, *ZAAC - J. Inorg.*
607 *Gen. Chem.* 431 (1977) 299–304. doi:10.1002/zaac.19774310134.
- 608 [43] X.Q. Tran, M. Hong, H. Maeno, Y. Kawami, T. Toriyama, K. Jack, Z.G. Chen, J. Zou, S.
609 Matsumura, M.S. Dargusch, Real-time observation of the thermally-induced phase
610 transformation in GeTe and its thermal expansion properties, *Acta Mater.* 165 (2019) 327–335.
611 doi:10.1016/j.actamat.2018.11.059.
- 612 [44] R. Shaltaf, E. Durgun, J.-Y. Raty, P. Ghosez, X. Gonze, Dynamical, dielectric, and elastic
613 properties of GeTe investigated with first-principles density functional theory, *Phys. Rev. B -*
614 *Condens. Matter Mater. Phys.* 78 (2008) 205203. doi:10.1103/PhysRevB.78.205203.
- 615 [45] H.L. Kagdada, P.K. Jha, P. Śpiewak, K.J. Kurzydłowski, Structural stability, dynamical
616 stability, thermoelectric properties, and elastic properties of GeTe at high pressure, *Phys. Rev.*
617 *B.* 97 (2018) 134105. doi:10.1103/PhysRevB.97.134105.
- 618 [46] R. Berthier, N. Bernier, D. Cooper, C. Sabbione, F. Hippert, P. Noé, *In situ* observation of the
619 impact of surface oxidation on the crystallization mechanism of GeTe phase-change thin films
620 by scanning transmission electron microscopy, *J. Appl. Phys.* 122 (2017) 115304.
621 doi:10.1063/1.5002637.
- 622 [47] P. Jost, H. Volker, A. Poitz, C. Poltorak, P. Zalden, T. Schäfer, F.R.L. Lange, R.M. Schmidt,
623 B. Holländer, M.R. Wirtsohn, M. Wuttig, Disorder-Induced Localization in Crystalline
624 Pseudo-Binary GeTe-Sb₂Te₃ Alloys between Ge₃Sb₂Te₆ and GeTe, *Adv. Funct. Mater.* 25
625 (2015) 6399–6406. doi:10.1002/adfm.201500848.
- 626 [48] K.N. Chen, C. Cabral, L. Krusin-Elbaum, Thermal stress effects of Ge₂Sb₂Te₅ phase change

- 627 material: Irreversible modification with Ti adhesion layers and segregation of Te,
628 Microelectron. Eng. 85 (2008) 2346–2349. doi:10.1016/j.mee.2008.09.009.
- 629 [49] J. Kalb, F. Spaepen, T.P.L. Pedersen, M. Wuttig, Viscosity and elastic constants of thin films
630 of amorphous Te alloys used for optical data storage Viscosity and elastic constants of thin
631 films of amorphous Te alloys used for optical data storage, J. Appl. Phys. 94 (2003) 4908.
632 doi:10.1063/1.1610775.
- 633 [50] M. Zhu, O. Cojocar-Mirédin, A.M. Mio, J. Keutgen, M. Küpers, Y. Yu, J.Y. Cho, R.
634 Dronskowski, M. Wuttig, Unique Bond Breaking in Crystalline Phase Change Materials and
635 the Quest for Metavalent Bonding, Adv. Mater. 1706735 (2018) 1–9.
636 doi:10.1002/adma.201706735.
- 637 [51] E. J. Mittemeijer, P. Scardi, Diffraction analysis of the microstructure of materials, Springer
638 Science & Business Media, 2003. doi:10.1007/978-3-662-06723-9.
- 639 [52] G.K. Williamson, W.H. Hall, X-RAY LINE BROADENING FROM FILED ALUMINIUM
640 AND WOLFRAM, Acta Metallurgica. 1 (1953) 22–31. doi:https://doi.org/10.1016/0001-
641 6160(53)90006-6.
- 642 [53] D.K. Hohnke, H. Holloway, S. Kaiser, PHASE RELATIONS AND TRANSFORMATIONS
643 IN THE SYSTEM PbTe-GeTe, J. Phys. Chem. Solids. 33 (1972) 2053–2062.
- 644 [54] A. V. Kolobov, J. Tominaga, P. Fons, T. Uruga, Local structure of crystallized GeTe films,
645 Appl. Phys. Lett. 82 (2003) 382–384. doi:10.1063/1.1539926.
- 646

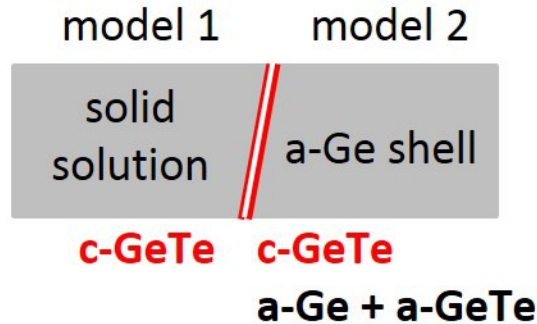


Temperature (°C)

$\text{a-Ge}_{0.52}\text{Te}_{0.48}$

$\Delta\sigma = +72 \text{ MPa}$

$T_x = 239^\circ\text{C}$



$\Delta\sigma = -54 \text{ MPa}$

$T_{\text{Ge}} = 297^\circ\text{C}$

